CHEMISTRY OF MATERIALS

pubs.acs.org/cm



Article

# Correlated Ion Transport Governed by Dynamic Local Structure in High Concentration and Localized High Concentration Electrolytes

Rohith Srinivaas Mohanakrishnan, Jingyang Wang, Joseph Park, and Kristin A. Persson*

Cite This: https://doi.org/10.1021/acs.chemmater.6c00541

Read Online

ACCESS | Metrics & More | Article Recommendations | Supporting Information



**ABSTRACT:** Understanding the dynamics of cluster formation and network percolation provides the mechanistic link between microscopic solvation structure and transport in concentrated electrolytes, including localized high-concentration electrolytes (LHCEs). Although recent studies have shown LHCEs to form micelle-like aggregates at specific compositions, a quantitative understanding of how solvation structures and transport properties depend on salt−solvent−diluent ratios remains limited. Here, we integrate molecular dynamics with Onsager transport analyses to chart the evolution of solvation microstructure and associated ionic transport in LiFSI/DMC/TTE, achieving good agreement with experimental conductivities across composition. We show that micelle formation arises from a dynamic instability of the cation−anion network, and that network percolation is the primary determinant of conductivity. Two compositional thresholds emerge: A critical network concentration (CNC) and a critical micelle concentration (CMC) that delineate transitions from extended percolating networks to micelle-like clusters and then to fragments. These structural transitions rationalize the nonintuitive conductivity decrease at intermediate dilution despite monotonically decreasing viscosity and provide composition-level design rules for LHCEs.

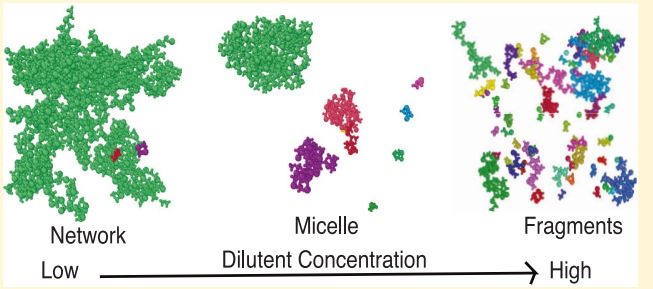


## INTRODUCTION

Ion clustering and network percolation in liquid electrolytes govern viscosity, conductivity, transference, and interphase chemistry, making structure−transport coupling a key design lever for energy technologies such as batteries, fuel cells, capacitors etc. Lithium-ion battery (LIB) technology is a prime example: While LIBs are foundational to sustainable energy storage, their performance is constrained by graphite anodes and intercalation-type cathodes.[1] To unlock higher capacities, e.g., lithium metal[2]/silicon[3] and next-generation cathodes[4] are being pursued, but these chemistries require tailored electrolyte formulations to minimize electrolyte breakdown, dendrite formation and parasitic reactivity.[5−10]

High-concentration electrolytes (HCEs; ≥4 M salt) favor anion-rich $Li^+$ solvation which generate more robust, inorganic-rich solid−liquid-electrolyte (SEI) interfaces, enhancing interfacial stability and oxidative resilience.[11−13] However, HCEs typically suffer from high viscosity, reduced ionic conductivity, and elevated cost.[11,14] Localized high-concentration electrolytes (LHCEs) aim to mitigate these drawbacks by introducing inert, nonsolvating diluents that are miscible with the solvent, preserving beneficial anion-rich solvation motifs while improving bulk transport and practicality through composition-controlled cluster formation and network percolation. Ideally, the diluent should have low viscosity, provide high permittivity without coordinating with the ions, remain inert and electrochemically stable and be nonflammable with low volatility.[7] Additives in this space such as 1,1,2,2-tetrafluoroethyl-2,2,3,3-tetrafluoropropyl ether (TTE) and *tris*(2,2,2-trifluoroethyl)orthoformate (TFEO) have been explored for their performance.[7,13]

Yet, recent research has shown that the relationship between LHCE composition and transport exhibits rich and nonintuitive behaviors. Bergström and McCloskey[12] investigated a prototypical LHCE comprising lithium bis(fluorosulfonyl)imide (LiFSI) salt, dimethyl carbonate (DMC) solvent, and TTE diluent. Using electrophoretic NMR and electrochemical characterization, they found that at 25 °C, in a 2.46 M LHCE (LiFSI:2DMC:1TTE), the product of molar ionic conductivity and viscosity decrease relative to the corresponding HCE (LiFSI:2DMC). This indicates that TTE is not an inert spacer but instead actively influences ion transport, motivating further microscopic evaluations of its role in solvation structure. Onsager analysis by the same authors suggested that these trends arose from nonideal ion−solvent interactions, indicating increased anticorrelated $Li^+$ motion and cation−anion drag

Received: February 20, 2026
Revised: June 25, 2026
Accepted: June 29, 2026

that disrupt long-lived structural diffusion ("hopping") pathways. Efaw et al.[13] further bridged macroscopic transport with nanoscale structures by examining LiFSI in dimethoxyethane (DME) with TFEO diluent. Combining MD simulations with Raman spectroscopy and small-/wide-angle X-ray scattering (SAX/WAX), they showed that above a critical concentration, TFEO drives the formation of micelle-like clusters—cation−anion dense aggregate cores in a TFEO matrix. The cation−anion aggregate fraction rises to ≈51% in the LHCE (vs ≈ 40% in the HCE without TFEO), locally concentrating salt and promoting LiF-rich SEI formation. Recent work by Hockmann et al.[15] has shed light on the internal interfaces that emerge within LHCEs due to nanoscale phase separation, providing key insights into how internal interfaces can modulate ion solvation and transport properties.

Previous studies have provided useful macroscopic observations but lack microscopic structural insights or broad compositional sampling. Key regions of the phase diagram remain unexplored, and notable features, such as the three-region conductivity profile in (LiFSI,DMC,TTE), have been reported but not connected to molecular interactions. Key questions remain regarding the salt−solvent−diluent phase space, particularly the precise conditions that induce micelle-like structuring and their impact on transport mechanisms. Here we comprehensively quantify key transport parameters, including viscosity, ionic conductivity, self- and cross-diffusion coefficients, and transference numbers, across a wide compositional range of the *x*LiFSI:*y*DMC:*z*TTE system (Figure 1).

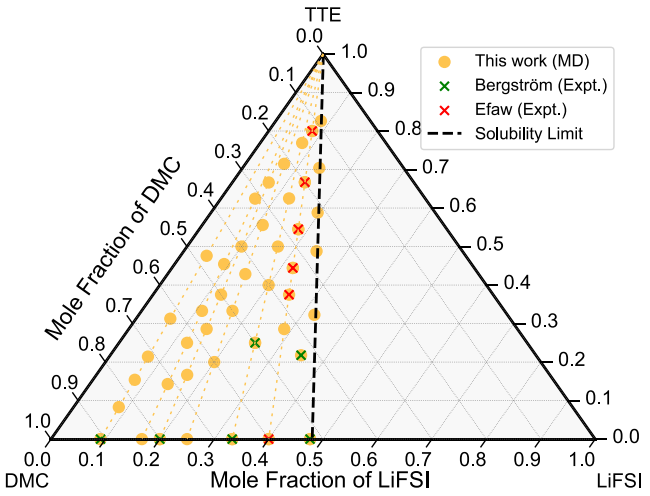


**Figure 1.** Explored LiFSI−DMC−TTE compositional space via MD simulations (yellow), with lines connecting points of constant LiFSI:DMC molar ratio. Overlaid are experimental data from Bergström & McCloskey(Reproduced from ref 12. Copyright 2024 American Chemical Society) and Efaw et al.(Adapted with permission from ref 13. Copyright 2023 Springer Nature). Black dotted line denote the solubility limit.[13]

The analyses conclusively demonstrate that micelle formation originates from a dynamic instability of the cation−anion network, with network percolation—rather than viscosity—governing ionic conductivity. The emergence of distinct critical network and micelle concentrations defines sharp structural transitions that explain the anomalous conductivity maximum at intermediate dilution and establish clear, composition-based design rules for LHCEs.

## METHODS

Molecular dynamics (MD) simulations were performed using LAMMPS[16] with the OPLS-AA force field[17] and literature-fitted parameters for LiFSI,[18] DMC,[19] and TTE.[20] Initial configurations were generated with PACKMOL.[21] Optimized Geometry and Atomic partial charges were obtained from DFT calculations (ORCA,[22] LC-BLYP(D4)/6−31++G(d,p) with range-separation parameter $\omega$ = 0.33 bohr$^{-1}$) followed by RESP analysis in Multiwfn,[23] and ionic charges were scaled by 0.72 to mitigate overestimated Coulomb interactions in nonpolarizable force fields.[24] The RESP fitted partial charges from the standard two-stage fitting procedure and reproduces the ESP with RRMSE less than 0.1 for all species. This value of charge scaling is based on the procedure followed by[25] and is obtained by benchmarking the MD conductivity, density and viscosity predictions from the Green−Kubo relations against experimental measurements from Table 1 in the Supporting Information.

## RESULTS AND DISCUSSION

### Solvation Structure

**Local Electrostatics.** To evaluate how the solvation structure influences the transport properties of the LiFSI-DMC-TTE system, we first examine local electrostatics by plotting the electrostatic potential of the anion ($FSI^-$), the solvent (DMC), and the diluent (TTE). In Figure 2, we infer that DMC can effectively solvate $Li^+$ and $FSI^-$ due to the presence of a highly positive electrostatic potential near its hydrogen atoms and the negative potential at the carbonyl oxygen, respectively. Notably, both these coordination environments remain accessible even under single bond rotations. In contrast, for TTE, the positive potential near its hydrogen atoms is electrostatically hindered by the electron-rich fluorine atoms, especially under single bond rotations, making a close approach to $FSI^-$ unfavorable. The electrostatic repulsion exists irrespective of the conformations of $FSI^-$ because of charge delocalization across the nitrogen and oxygens. Additionally, TTE's deeply electron-poor ether oxygen has minimal Lewis basicity, and its low polarity offers insufficient stabilization for $Li^+$.

**Solvation Environment and Residence Time.** Radial distribution functions provided in Figure S4(Supporting Information S4) reveal that the first and second coordination shells around $Li^+$ are populated exclusively by the anion ($FSI^-$) and solvent (DMC). In contrast, the diluent (TTE) has negligible presence in the first solvation shell of $Li^+$, with absence of a discernible first-shell peak in the $Li^+$−TTE radial distribution function which further confirms that TTE does not form a well-defined coordination environment around $Li^+$. These findings reflect the electrostatic tendency of DMC to engage in local interactions with $Li^+$ and $FSI^-$. Since a single $FSI^-$ can coordinate with multiple $Li^+$ ions, we classify $FSI^-$ coordination environment into four categories: solvent-separated ion pairs (SSIP) with 0 $Li^+$, contact ion pairs (CIP) with 1 $Li^+$, aggregates (AGG) with 2 or 3 $Li^+$, and overcoordinated aggregates ($AGG^+$) with 4 or more $Li^+$.[13]

Figure 3a−d presents the variation of the fractions of SSIP, CIP, AGG, and $AGG^+$ with increasing DMC:LiFSI at each fixed TTE:LiFSI. As DMC becomes more abundant, $Li^+$−$FSI^-$ coordination gradually gives way to $FSI^-$− DMC solvation, evidenced by the drop in the $AGG^+$ fraction between DMC: LiFSI = 1.1 and 2 at all amounts of TTE. Because $AGG^+$ cores, surrounded by AGG, underpin larger assemblies (networks[19] or micelle-like clusters), their disappearance beyond DMC:LiFSI > 2 demonstrates that such


https://doi.org/10.1021/acs.chemmater.6c00541
Chem. Mater. XXXX, XXX, XXX−XXX

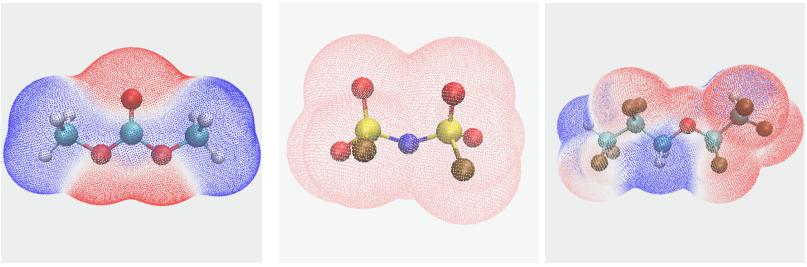

(a) DMC (b) $FSI^-$ (c) TTE

**Figure 2.** Molecular van der Waals (vdW) surface map of (a) DMC (b) $FSI^-$ (c) TTE colored according to the electrostatic potential. Red represents the minima in the electrostatic potential whereas blue represents the maxima in the electrostatic potential. Atoms are represented in the following color scheme: Red: Oxygen, Blue: Carbon, White: Hydrogen, Yellow: Sulfur, Purple: Nitrogen, Brown: Flourine.

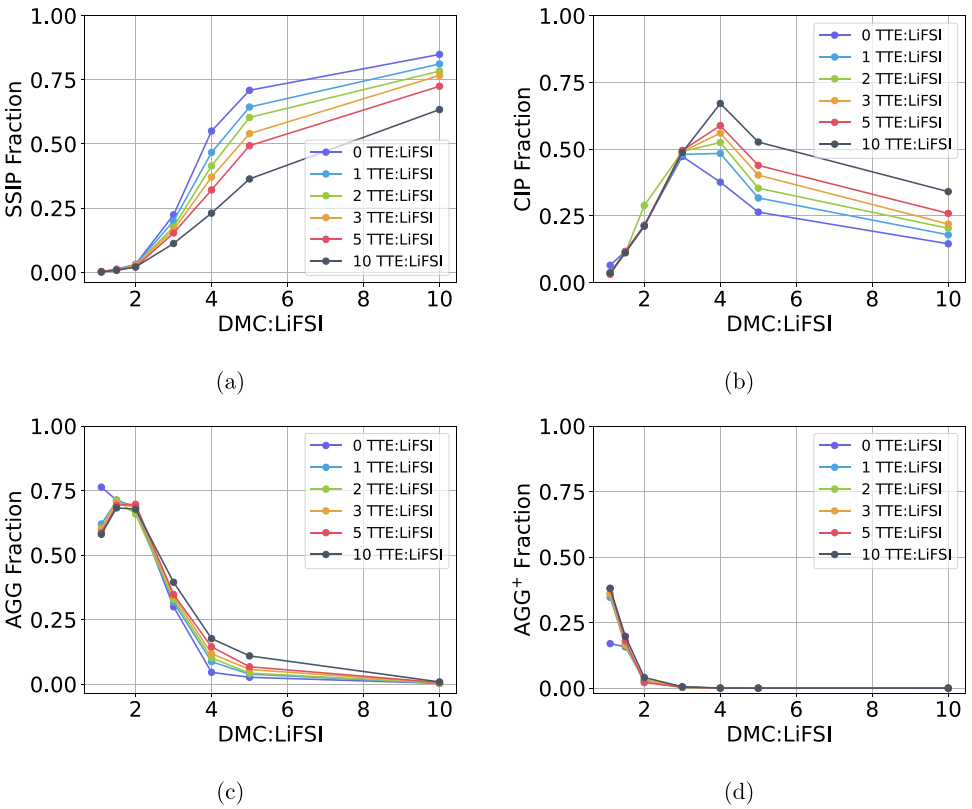


**Figure 3.** Fraction of $FSI^-$ in (a) SSIP (b) CIP (c) AGG (d) $AGG^+$ solvation environment, for a range of different concentrations as a function of solvent-salt molar ratio ($x$-axis) and diluent-salt molar ratio (legend).

structures only persist at DMC:LiFSI $\leq$ 2, independently of TTE content. Likewise, the DMC content and its ability to solvate ions dictate the primary solvation environment, with AGG dominating at DMC:LiFSI $\leq$ 2, CIP dominating for 2 < DMC:LiFSI < 4, and SSIP dominating at DMC:LiFSI > 4, as illustrated in Figure 4. Based on dominating primary solvation environment, we classify the solvation regime as **solvent-in-salt**—AGG dominating; **salt-solvate**—CIP dominating and **salt-in-solvent**—SSIP dominating regimes. However, the effect of TTE is not as straightforward. A preliminary assessment based on coordination numbers indicates that the increase in the TTE content increases the fraction of CIP while decreasing the fraction of SSIP both in salt-solvate and salt-in-solvent regimes. This observation is consistent with the literature, which reports that the fraction of free solvent molecules increases as the concentration of the diluent increases.[26] Yet, this effect is not pronounced in the solvent-in-salt regime where the addition of TTE shows a distinct increase in AGG+ at the expense of AGG in the system.

To identify the effect of TTE, we evaluate the residence time, which measures how long a species stays near an ion on average, and the bound time, which captures the uninterrupted duration of that close association (Figure S5, Supporting Information S5). The ratio of bound time and residence time provides information on the extent of concerted ion-hopping between species $i$ and species $j$.[27] Figure 5b demonstrates that in the solvent-in-salt regime, $Li^+$ and DMC do not show any concerted "ion-hopping" behavior. Based on Figure 5a subject to the studied concentration range, the presence or absence of TTE determines the change in $Li^+$—$FSI^-$ interaction. In the solvent-in-salt regime, $FSI^-$ and TTE come closer ($\approx$ 3.85 Å), but local electrostatic repulsion drives $FSI^-$ to shift toward neighboring $Li^+$ ions to avoid TTE proximity. This triggers a cascading exchange of ligands($FSI^-$ displacing DMC & $FSI^-$


https://doi.org/10.1021/acs.chemmater.6c00541
Chem. Mater. XXXX, XXX, XXX−XXX

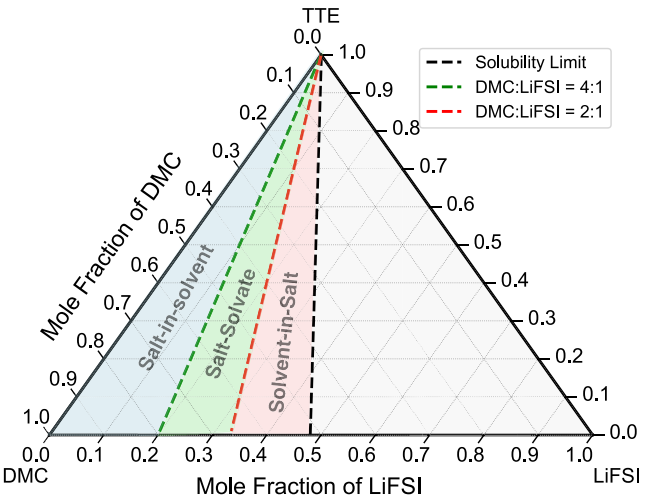


**Figure 4.** Various solvation regimes across the LiFSI:DMC:TTE compositional space. The solvent-in-salt regime is shaded in red, the salt-solvate regime in green and the salt-in-solvent is shaded in blue.

displacing $FSI^-$) between adjacent $Li^+$ ions, as each $Li^+$ can coordinate only 4 ligands on average. From Figure 5a, it can be observed that the ratio of bound time to residence time for the $Li^+$-$FSI^-$ pair changes from 6.27 to 0.97 when 1 TTE is added to LiFSI-1.1DMC. As this ratio directly relates to the number of concerted ion-hopping steps, this shows the disruption of concerted ion-transport due to the presence of TTE.

**Higher Order Structures and Lifetime.** Large fractions of AGG in the solvent-in-salt regime suggests the presence of higher order structures containing $Li^+$ and $FSI^-$ ions. Efaw et al.[13] identified these higher-order structures as micelles and fragments, with micelles characterized by a high $AGG^+/AGG$ ratio, and fragments arising from the disintegration of micelles. The definition and the characterization from Efaw et al.[13] is based on the ion-rich core−shell framework in which the solvent acts as a good surfactant, binding the immiscible salt and diluent phases, reducing the interfacial energy in order to stabilize the dispersed liquid microstructure. However, this definition does not distinguish between percolating and nonpercolating structures which is critical to understand the overall transport properties. Hence we characterize these higher order structures including their percolating behavior along with ion-rich core−shell model as follows: **Networks**—percolating structures with ion-rich core−shell framework, **micelles**—nonpercolating structures with ion-rich core−shell framework, and **fragments**—nonpercolating structures without ion-rich core−shell framework as shown in Figure 6. The $AGG^+/AGG$ ratio suggested by Efaw et al.[13] does not differentiate between network and micelle as both contain a large $AGG^+$ core with an AGG outer shell. We represent these higher-order structures using a graph formalism, where $Li^+$ and $FSI^-$ ions serve as the nodes and the $Li^+$−$FSI^-$ solvation radius defines the edge weights. This construction allows us to compute the graph diameter, which corresponds to the longest possible connected pathway of ions within a given structure.The graph diameter is computed using unwrapped atomic coordinates, such that it reflects the true physical end-to-end distance of the ion cluster in real space. When this unwrapped pathway extends longer than the simulation box length, the structure is deemed percolating, thereby forming a continuous conductive network that enables efficient long-range ion transport. We refer to the calculated graph diameter as the length of the higher-order structure, since it quantifies the physical distance over which connectivity is maintained. Subsequently, we calculate the structure lengths, number of $Li^+$ ions and lifetimes, normalized by the length of cubic simulation box, the total number of the $Li^+$ ions and the residence time of the $Li^+$-$FSI^-$ pair at the relevant concentration (Supporting Information S6), respectively. Hereafter, the term "length" denotes the normalized length, "$Li^+$ amount" refers to the normalized $Li^+$ amount, and "lifetime" refers to the normalized lifetime.

The length of the higher-order structures govern their percolation behavior, following the order: networks ≫ micelles > fragments. Similarly, the $Li^+$ content within these structures reflects the extent of ion-rich core−shell organization, in the order: Networks > micelles ≫ fragments. The lifetime further provides insight into how different higher-order structures coexist. (Figure 7a) shows that at low diluent content (TTE:LiFSI < 5), the structure length is percolating across the longest dimension of the simulation box (diagonal). In contrast, at high diluent content (TTE:LiFSI > 5), the length falls below 1.0 and exhibits a bimodal distribution. A similar trend is observed in (Figure 7b) for $Li^+$ content: values remain close to 1.0 at low diluent content, while at higher diluent content (TTE:LiFSI > 5) a bimodal distribution emerges. These results clearly indicate that network formation is favored

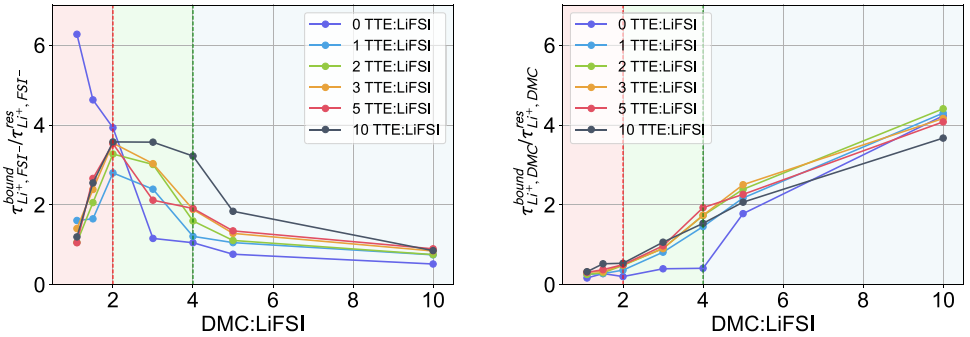


**Figure 5.** Ratio of bound time to residence time of (a) $Li^+$-$FSI^-$ (b) $Li^+$-DMC pairs as a function of different concentrations with solvent-salt molar ratio (*x*-axis) and diluent-salt molar ratio (legend) concentrations. Solvent-in-Salt (red), Salt-Solvate (green) and Salt-in-Solvent (blue) regimes are highlighted.


https://doi.org/10.1021/acs.chemmater.6c00541
Chem. Mater. XXXX, XXX, XXX−XXX

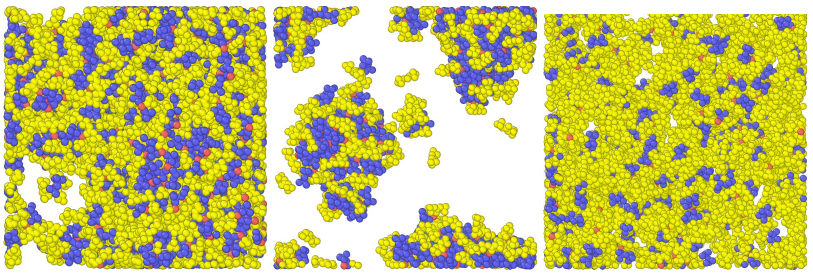


**Figure 6.** Representative snapshots from MD simulations of $Li^+/FSI^-$ clusters, showing three distinct higher order structures: (a) Network—an extended, percolating network of aggregates; (b) Micelle—a compact, micelle−like assembly; (c) Fragment—a small, nonpercolating chain. Yellow—DMC, Blue—$FSI^-$, Red—$Li^+$, Empty space—TTE.

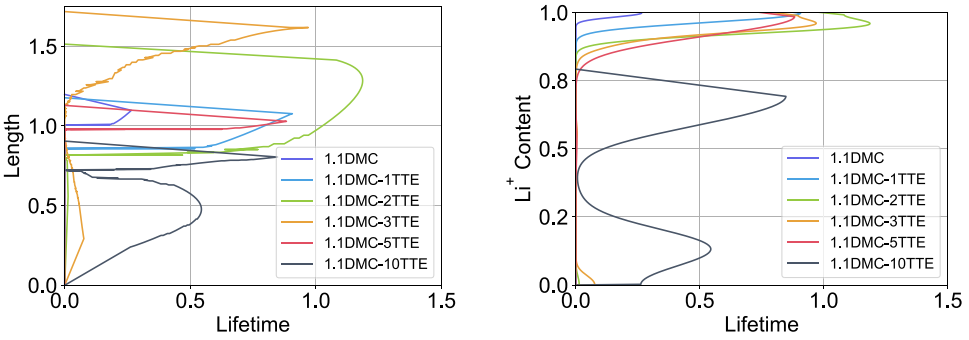


**Figure 7.** Characteristics of higher order solvation structures for DMC:LiFSI = 1.1 with varying TTE content. Specifically (a) Length (normalized) as a function of its lifetime (normalized) and (b) $Li^+$ content (normalized) as a function of its lifetime (normalized).

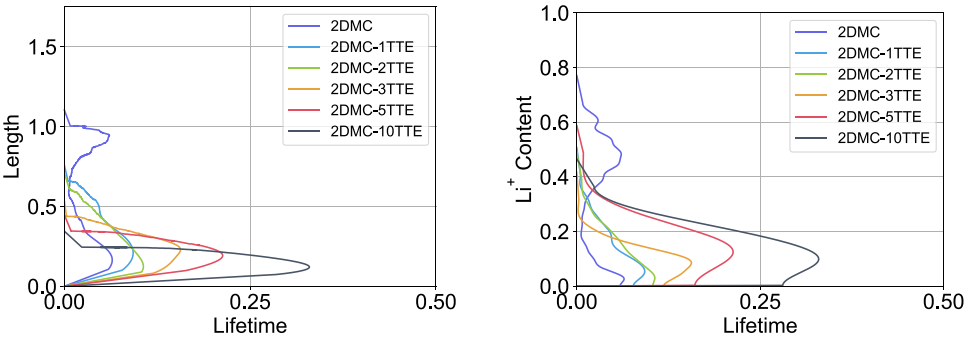


**Figure 8.** Characteristics of higher order solvation structures for DMC:LiFSI = 2 with varying TTE content. Specifically (a) Length (normalized) as a function of its lifetime (normalized) and (b) $Li^+$ content (normalized) as a function of its lifetime (normalized).

at low diluent content. At higher diluent content, however, the observed bimodal distributions of both length and $Li^+$ content is attributed to the thermodynamic coexistence of micelles and fragments. Such coexistence is well established through the molecular thermodynamic framework of surfactant self-assembly,[28,29] where the aggregate size distribution contains finite contributions from both small fragments and micelles, leading to bimodal behavior. Accordingly, as the diluent content increases, the dominant higher-order structure evolves from networks to a state characterized by the coexistence of micelles and fragments. We define this transition point as the **Critical Network Concentration(CNC)** limit.

As shown in Figure 4, DMC:LiFSI = 2 lies at the solvent-in-salt/salt-solvate boundary where, in the absence of TTE, the length distribution is bimodal. Introducing TTE at this composition induces higher-order structural reorganization: The length of the higher order structure falls below 1.0 for all TTE contents examined, and the distribution collapses to a unimodal peak with a mean of 0.2 (Figure 8a). A similar trend for $Li^+$ clustering is observed in (Figure 8b) where a bimodal distribution is observed in the absence of TTE, while with TTE addition, a unimodal distribution with a mean cluster $Li^+$ content of 0.1. These results indicate that, in the absence of TTE, coexistence of micelle and fragments is favored whereas fragment formation is favored with TTE addition. The concentration in which micelle disintegrate to form fragments is referred as the **Critical Micelle Concentration(CMC)** limit which agrees well with the existing definition from Efaw et al.[13] The results from DMC:LiFSI = 1.1 and DMC:LiFSI = 2 further reveal that the effect of diluent addition on these


https://doi.org/10.1021/acs.chemmater.6c00541
Chem. Mater. XXXX, XXX, XXX−XXX

structures is strongly dependent on the solvent content of the electrolyte. Notably, the direct transition from extended networks to a coexistence state of micelles and fragments beyond the CNC indicates that micelles persist only in dynamic equilibrium with a finite population of fragments.

## Transport Properties

**Viscosity and Diffusion Coefficients.** Based on Figure 9, the viscosity decreases with both the addition of TTE and

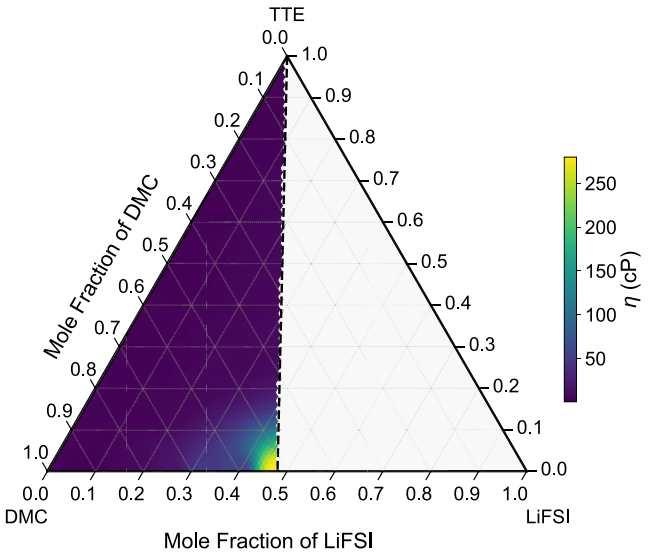


**Figure 9.** Computed viscosity for the LiFSI-DMC-TTE compositional space.

DMC with a maximum viscosity of 280 cP observed at LiFSI:1.1DMC. Contour corresponding to 10 cP, intersects the solubility line at LiFSI:1.1DMC:1TTE and the LiFSI-DMC binary at LiFSI:4DMC respectively. This shows that nearly 3 DMC:LiFSI is required if only DMC is used for additional dilution, whereas 1 TTE:LiFSI is required if only TTE is used for additional dilution. Thus, TTE acts as an effective dilutent compared to DMC by breaking the networks in the solvent-in-salt regime without participating in the solvation environment of the salt.

The diffusion coefficient of $Li^+$, $FSI^-$, DMC, TTE are plotted in Figure S3 (Supporting Information S2). As expected the diffusion coefficient of all species increases with the addition of TTE. Among the species, the diffusion coefficient of TTE is highest, followed by DMC and $FSI^-$ with $Li^+$ having the lowest diffusion coefficients. The addition of TTE in the salt-in-solvent regime shows minimal improvement in the viscosity and diffusion coefficients. This is because in the salt-in-solvent regime, the higher order structures are absent due to low fractions of AGG and hence the effect of TTE is negligible.

**Conductivity.** As shown in (Figure 10a), adding TTE decreases both the electrolyte conductivity and viscosity (see Figure 9). To investigate the microscopic origin of this behavior, we evaluate both the ideal and nonideal components of conductivity using Onsager transport coefficients. Based on (Figure 10b), we find that the nonideal contribution to conductivity becomes negative in the presence of TTE. The ideal conductivity remains positive and increases with TTE content. This increase arises because the ideal conductivity, derived from the sum of the $Li^+$ and $FSI^-$ diffusion coefficients, reflects the enhanced ion diffusion with TTE addition (see Figure S3, Supporting Information S2). In contrast, the nonideal component, which is based on distinct Onsager transport coefficients, decreases, indicating stronger ion−ion correlations that reduce net charge transport. The per-ion $L^{+,-}$ Onsager transport coefficient is shown in (Figure 10c), while $L^{+,+}_{dist}$ and $L^{-,-}_{dist}$ are provided in the Figure S2(Supporting Information S2). All three coefficients increase with TTE addition, with the steepest rise occurring in the solvent-in-salt regime, followed by the salt-solvate regime. Within the salt-in-solvent regime, TTE has little effect because LiFSI is fully solvated by DMC. By contrast, in the solvent-in-salt regime, TTE perturbs the local $FSI^-$ environment and triggers a cascade of ion displacements. Because $Li^+$−$FSI^-$ interactions are predominantly Coulombic, this perturbation strengthens long-range ionic correlations, increasing all three per-ion transport coefficients with added TTE.

The mean $Li^+$−$FSI^-$ separation (2.59 Å) is markedly shorter than the corresponding like-ion separations (3.80 Å), which preferentially amplifies $L^{+,-}$ relative to $L^{+,+}_{dist}$ and $L^{-,-}_{dist}$. This asymmetry drives a more negative nonideal contribution to the conductivity, which grows in magnitude with increasing TTE. Based on (Figure 10c), in the absence of TTE, the per-ion $L^{+,-}$ increases slightly with the addition of DMC. This trend aligns with electrophoretic NMR measurements reported by Bergstrom and co-workers.[12] The increase in per-ion $L^{+,-}$ when DMC is added in the absence of TTE, is due to the characteristic diffusion length (Supporting Information S7) which represents the average distance two ions diffuse together before drifting apart. The characteristic diffusion length of the $Li^+$-$FSI^-$ pair increases from 5.63 Å to 7.15 Å as the DMC:LiFSI ratio increases from 1.1 to 10. Additionally, the product of $k_{min}\left(=\frac{2\pi}{A}\right)$ and $\zeta$ is less than 1.0 for all compositions where $A$ is the simulation box length and $\zeta$ is the correlation length(Supporting Information S3). This suggests the that long-wavelength concentration fluctuations are fully contained within the simulation box, and that the Onsager transport coefficients remain valid even when the higher order structures are present. To examine the relationship between ion transport and higher-order structure in the solvent-in-salt regime, we compare our computed ionic conductivities for the LiFSI-1.5DMC-$x$TTE ($x$ = 0−10) system with experimental measurements by Efaw et al.[13] As shown in (Figure 11a), the agreement between simulation and experiment is remarkable. Based on (Figure 11b), it can be observed that in the absence of TTE, the length of the higher order structure extends to the size of the simulation box and hence networks are the dominant higher order structures. However, when $x$ exceeds 2 (CNC limit), conductivity drops sharply due to the formation of micelles, which are characterized by a bimodal distribution in length and $Li^+$ content. Upon further increase of $x$ beyond 10 (CMC limit), fragment formation emerges (Figure 11b). Fragmentation is accompanied by poor conductivity, underscoring the key role of the CMC in LHCE design. To reduce viscosity without sacrificing conductivity, the electrolyte composition must remain within the CNC regime, where the network structure is preserved and $Li^+$ transport remains efficient.

**Transference Number and Mode of Transport.** Figure 12 a,b presents the true $Li^+$ transference number in the center-of-mass (CM) frame of reference and the $Li^+$ ion transport mode analysis, respectively. Based on (Figure 12a), the true $Li^+$ transference number ($t^{CM}_{Li^+}$) decreases from 0.60 to 0.34 as the


https://doi.org/10.1021/acs.chemmater.6c00541
Chem. Mater. XXXX, XXX, XXX−XXX

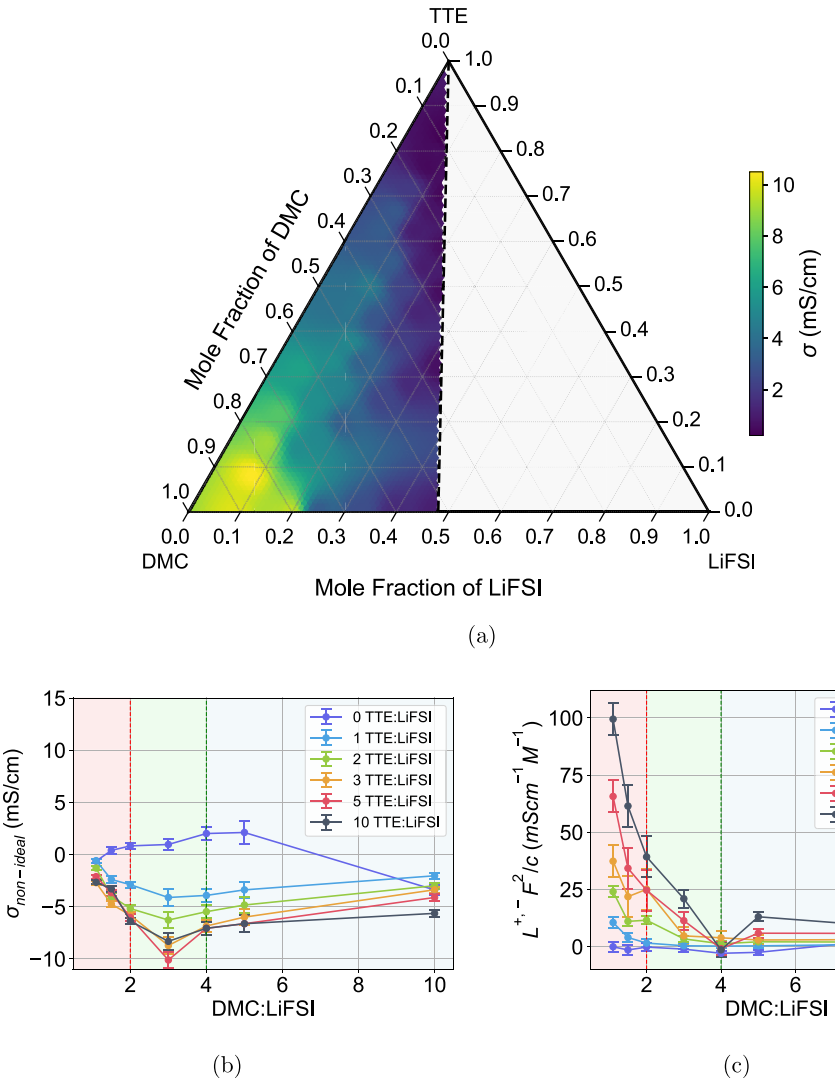


**Figure 10.** (a) Conductivity (b) Nonideal Conductivity (c) Per-ion $L^{+,-}$ Onsager transport coefficient. Solvent-in-Salt (red), Salt-Solvate (green) and Salt-in-Solvent (blue) regimes are highlighted.

DMC:LiFSI ratio increases from 1.1 to 10. In the absence of TTE, the relatively high $t_{Li^+}^{CM}$ observed in the solvent-in-salt regime arises from network formation. At low to intermediate TTE content (1 < TTE:LiFSI < 10), $t_{Li^+}^{CM}$ drops sharply in the solvent-in-salt regime. This reduction is attributed to the cascading displacement effect, where TTE locally repels $FSI^-$, enhancing its mobility relative to $Li^+$. At TTE:LiFSI $\geq$ 10, the structure is dominated by fragments, not ion-rich networks or micelles. The resulting absence of a core−shell architecture suppresses the selective displacement of $FSI^-$ driven by local TTE repulsion, which elevates $Li^+$ mobility relatively and increases $t_{Li^+}^{CM}$.

The ratio of the characteristic diffusion length($L_{ij}^c$) to the length scale relevant to the solvation shell($R_{ij}^S + 2R_j^g$) helps to identify the mode of transport (Supporting Information S7). If this ratio is less than 1.0, the dominant ion-transport mechanism is structural; if it exceeds 1.0, the ion-transport is predominantly vehicular.[27] Based on (Figure 12 b), in the absence of TTE, the motion of $Li^+$ is structural relative to $FSI^-$ (<1.0). Any addition of TTE makes the motion of $Li^+$ vehicular relative to both $FSI^-$(>1.0) even in the solvent-in-salt regime where networks are the predominant higher order structures. This suggests that vehicular motion of $Li^+$ with respect to $FSI^-$ is possible even in the presence of networks. A similar analysis on the mode of transport of $Li^+$ relative to DMC exhibits vehicular behavior as shown in the Figure S6(Supporting Information S7).

## SUMMARY

We have elucidated the molecular-level mechanisms governing ion transport in localized high-concentration electrolytes (LHCEs) through systematic simulation and experimental validation of the (LiFSI,DMC,TTE) ternary system. By analyzing transport coefficients, solvation dynamics, and clustering behavior across a wide compositional range, we reveal that the transition from a percolated network to a micelle-dominated regime fundamentally limits ionic conductivity in dilute LHCEs. Our analysis reveals two transport-controlling structural thresholds: A critical network concentration (CNC), marking the onset of collapse of the percolating ion−ion network, and a critical micelle concentration (CMC), above which surfactant-like micelles disintegrate into fragments. The CMC is in close accord with Efaw et al.'s recent observations, including a remarkable agreement with their measured conductivity as a function of salt


https://doi.org/10.1021/acs.chemmater.6c00541
Chem. Mater. XXXX, XXX, XXX−XXX

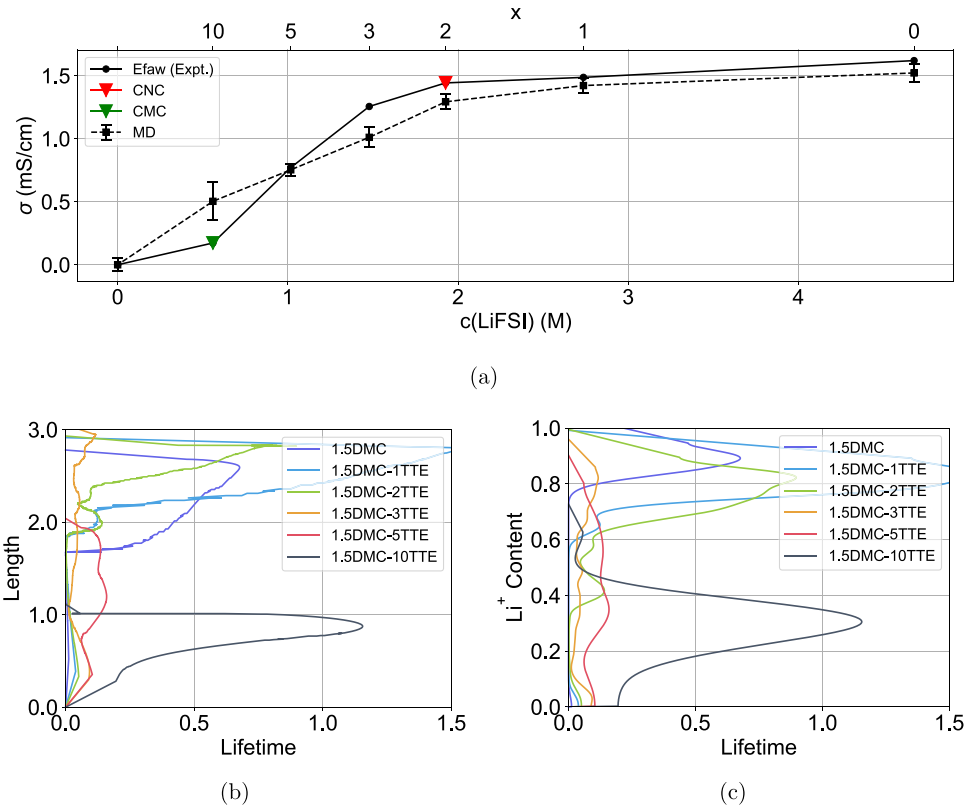


**Figure 11.** (a) Experimentally measured(Adapted with permission from ref 13 Copyright 2023 Springer Nature) and computed ionic conductivity for LiFSI-1.5DMC-*x*TTE as a function of salt concentration; TTE content shown on the secondary *x*-axis. Characteristics of higher order solvation structures for DMC:LiFSI = 1.5 with varying TTE content. Specifically (b) Length (normalized) as a function of its lifetime (normalized) and (c) $Li^+$ content (normalized) as a function of its lifetime (normalized).

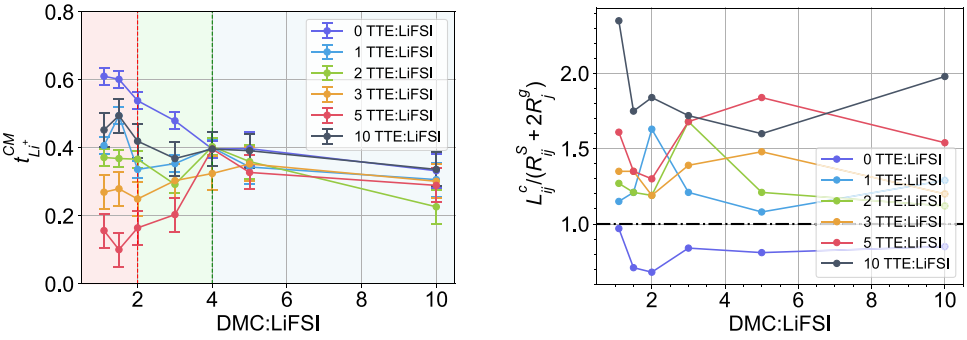


**Figure 12.** (a) True $Li^+$ transference number (b) Mode of Transport Analysis for $Li^+$-$FSI^-$. Solvent-in-Salt (red), Salt-Solvate (green) and Salt-in-Solvent (blue) regimes are highlighted.

composition. Beyond the CNC, TTE disrupts percolation and induces micelles, leading to short-lived free carriers and strong ion−ion anticorrelations, thereby depressing conductivity. These effects suppress collective ionic conductivity despite increased self-diffusion, explaining the experimentally observed sharp decrease in conductivity at intermediate diluent concentrations. Our findings clarify the physical origin of conductivity decrease in LHCEs and provide a mechanistic framework for interpreting ion transport in complex electrolyte systems. By distinguishing between structural and vehicular transport modes and tracking solvation motif transitions, this work also offers actionable guidelines for electrolyte formulation: optimal performance occurs near the CNC, before micelle formation impairs long-range charge transport. Our analysis is broadly applicable to other salt−solvent−diluent systems and improves design toward electrolytes that balance local coordination, long-range connectivity, and dynamic stability.

## ■ ASSOCIATED CONTENT

### Supporting Information

The Supporting Information is available free of charge at https://pubs.acs.org/doi/10.1021/acs.chemmater.6c00541.

Molecular dynamics simulation details; Green−Kubo transport property calculations; correlation length



https://doi.org/10.1021/acs.chemmater.6c00541
Chem. Mater. XXXX, XXX, XXX−XXX

analysis; benchmark comparison with experimental data; radial distribution functions; residence time and bound time definitions; higher-order structure length and lifetime methodology; mode of transport analysis (PDF)

## AUTHOR INFORMATION


### Corresponding Author

**Kristin A. Persson** − *Department of Materials Science and Engineering, University of California Berkeley, Berkeley, California 94720, United States; Materials Sciences Division, Lawrence Berkeley National Laboratory, Berkeley, California 94720, United States;* orcid.org/0000-0003-2495-5509; Email: kapersson@lbl.gov

### Authors

**Rohith Srinivaas Mohanakrishnan** − *Department of Materials Science and Engineering, University of California Berkeley, Berkeley, California 94720, United States; Materials Sciences Division, Lawrence Berkeley National Laboratory, Berkeley, California 94720, United States;* orcid.org/0000-0003-1898-0660

**Jingyang Wang** − *Key Laboratory of Theoretical & Computational Photochemistry of Ministry of Education, College of Chemistry, Beijing Normal University, Beijing 100875, People's Republic of China*

**Joseph Park** − *Materials Sciences Division, Lawrence Berkeley National Laboratory, Berkeley, California 94720, United States; Department of Chemical and Biomolecular Engineering, University of California Berkeley, Berkeley, California 94720, United States*

Complete contact information is available at: https://pubs.acs.org/10.1021/acs.chemmater.6c00541


### Author Contributions

R.S.M. and K.A.P. conceived the scientific direction. R.S.M. wrote the analysis codes. J.W. performed the simulations. R.S.M., J.P., and K.A.P. wrote the manuscript. All authors discussed the results and provided further edits to the paper.

### Notes

The authors declare no competing financial interest.

## ACKNOWLEDGMENTS

R.S.M., J.W., J.P., and K.A.P gratefully acknowledge support by the Assistant Secretary for Energy Efficiency and Renewable Energy, Office of Vehicle Technologies of the U.S. Department of Energy under Contract DE-AC02-05CH11231 through the Disordered Rocksalt (DRX+) Program. R.S.M was also supported in part by the Jane Lewis Fellowship at UC Berkeley.

## REFERENCES


(1) Li, L.; Wang, Z. H.; Jiang, G. X. Hydrothermal Synthesis of $Fe_3O_4$@C Spheres as Anode Material for Lithium-Ion Batteries. *Solid State Phenom.* **2018**, *281*, 801−806.

(2) Whittingham, M. S. History, Evolution, and Future Status of Energy Storage. *Proc. IEEE* **2012**, *100*, 1518−1534.

(3) Xu, K. Electrolytes and Interphases in Li-Ion Batteries and Beyond. *Chem. Rev.* **2014**, *114*, 11503−11618.

(4) Hau, H.; Holstun, T.; Lee, E.; Rinkel, B. L. D.; Mishra, T. P.; Markuson DiPrince, M.; Mohanakrishnan, R. S.; Self, E. C.; Persson, K. A.; McCloskey, B. D.; Ceder, G. Disordered Rocksalts as High-Energy and Earth-Abundant Li-Ion Cathodes. *Adv. Mater.* **2025**, *37*, No. 2502766.

(5) Qian, J.; Henderson, W. A.; Xu, W.; Bhattacharya, P.; Engelhard, M.; Borodin, O.; Zhang, J.-G. High rate and stable cycling of lithium metal anode. *Nat. Commun.* **2015**, *6*, No. 6362.

(6) Suo, L.; Hu, Y.-S.; Li, H.; Armand, M.; Chen, L. A new class of Solvent-in-Salt electrolyte for high-energy rechargeable metallic lithium batteries. *Nat. Commun.* **2013**, *4*, No. 1481.

(7) Yamada, Y.; Wang, J.; Ko, S.; Watanabe, E.; Yamada, A. Advances and issues in developing salt-concentrated battery electrolytes. *Nat. Energy* **2019**, *4*, 269−280.

(8) Seo, D. M.; Reininger, S.; Kutcher, M.; Redmond, K.; Euler, W. B.; Lucht, B. L. Role of Mixed Solvation and Ion Pairing in the Solution Structure of Lithium Ion Battery Electrolytes. *J. Phys. Chem. C* **2015**, *119*, 14038−14046.

(9) Borodin, O.; Self, J.; Persson, K. A.; Wang, C.; Xu, K. Uncharted Waters: Super-Concentrated Electrolytes. *Joule* **2020**, *4*, 69−100.

(10) Suo, L.; Borodin, O.; Wang, Y.; Rong, X.; Sun, W.; Fan, X.; Xu, S.; Schroeder, M. A.; Cresce, A. V.; Wang, F.; Yang, C.; Hu, Y.; Xu, K.; Wang, C. "Water-in-Salt" Electrolyte Makes Aqueous Sodium-Ion Battery Safe, Green, and Long-Lasting. *Adv. Energy Mater.* **2017**, *7*, No. 1701189.

(11) Chen, S.; Zheng, J.; Mei, D.; Han, K. S.; Engelhard, M. H.; Zhao, W.; Xu, W.; Liu, J.; Zhang, J. High-Voltage Lithium-Metal Batteries Enabled by Localized High-Concentration Electrolytes. *Adv. Mater.* **2018**, *30*, No. 1706102.

(12) Bergstrom, H. K.; McCloskey, B. D. Ion Transport in (Localized) High Concentration Electrolytes for Li-Based Batteries. *ACS Energy Lett.* **2024**, *9*, 373−380.

(13) Efaw, C. M.; Wu, Q.; Gao, N.; et al. Localized high-concentration electrolytes get more localized through micelle-like structures. *Nat. Mater.* **2023**, *22*, 1531−1539.

(14) Ren, X.; Chen, S.; Lee, H.; et al. Localized High-Concentration Sulfone Electrolytes for High-Efficiency Lithium-Metal Batteries. *Chem.* **2018**, *4*, 1877−1892.

(15) Hockmann, A.; Schönhoff, M.; Diddens, D. Analyzing the internal interface in localized high-concentration electrolytes. *J. Chem. Phys.* **2025**, *163*, No. 084719, DOI: 10.1063/5.0285201.

(16) Thompson, A. P.; Aktulga, H. M.; Berger, R.; Bolintineanu, D. S.; Brown, W. M.; Crozier, P. S.; in 't Veld, P. J.; Kohlmeyer, A.; Moore, S. G.; Nguyen, T. D.; Shan, R.; Stevens, M. J.; Tranchida, J.; Trott, C.; Plimpton, S. J. LAMMPS - a flexible simulation tool for particle-based materials modeling at the atomic, meso, and continuum scales. *Comput. Phys. Commun.* **2022**, *271*, No. 108171.

(17) Jorgensen, W. L.; Maxwell, D. S.; Tirado-Rives, J. Development and Testing of the OPLS All-Atom Force Field on Conformational Energetics and Properties of Organic Liquids. *J. Am. Chem. Soc.* **1996**, *118*, 11225−11236.

(18) Sambasivarao, S. V.; Acevedo, O. Development of OPLS-AA Force Field Parameters for 68 Unique Ionic Liquids. *J. Chem. Theory Comput.* **2009**, *5*, 1038−1050.

(19) Perez Beltran, S.; Cao, X.; Zhang, J.-G.; Balbuena, P. B. Localized High Concentration Electrolytes for High Voltage Lithium-Metal Batteries: Correlation between the Electrolyte Composition and Its Reductive/Oxidative Stability. *Chem. Mater.* **2020**, *32*, 5973−5984.

(20) Kim, S. C.; Wang, J.; Xu, R.; et al. High-entropy electrolytes for practical lithium metal batteries. *Nat. Energy* **2023**, *8*, 814−826.

(21) Martínez, L.; Andrade, R.; Birgin, E. G.; Martínez, J. M. PACKMOL: A package for building initial configurations for molecular dynamics simulations. *J. Comput. Chem.* **2009**, *30*, 2157−2164.

(22) Neese, F.; Wennmohs, F.; Becker, U.; Riplinger, C. The ORCA quantum chemistry program package. *J. Chem. Phys.* **2020**, *152*, No. 224108, DOI: 10.1063/5.0004608.

(23) Lu, T.; Chen, F. Multiwfn: A multifunctional wavefunction analyzer. *J. Comput. Chem.* **2012**, *33*, 580−592.

(24) Leontyev, I.; Stuchebrukhov, A. Accounting for electronic polarization in non-polarizable force fields. *Phys. Chem. Chem. Phys.* **2011**, *13*, 2613−2626.
(25) Li, Z.; Robertson, L. A.; Shkrob, I. A.; Smith, K. C.; Cheng, L.; Zhang, L.; Moore, J. S.; Z, Y. Realistic Ion Dynamics through Charge Renormalization in Nonaqueous Electrolytes. *J. Phys. Chem. B* **2020**, *124*, 3214−3220.
(26) Ren, F.; Li, Z.; Chen, J.; Huguet, P.; Peng, Z.; Deabate, S. Solvent-Diluent Interaction-Mediated Solvation Structure of Localized High-Concentration Electrolytes. *ACS Appl. Mater. Interfaces* **2022**, *14*, 4211−4219.
(27) Self, J.; Fong, K. D.; Persson, K. A. Transport in Superconcentrated LiPF6 and LiBF4/Propylene Carbonate Electrolytes. *ACS Energy Lett.* **2019**, *4*, 2843−2849.
(28) Nagarajan, R.; Ruckenstein, E. Theory of Surfactant Self-Assembly: A Predictive Molecular Thermodynamic Approach. *Langmuir* **1991**, *7*, 2934−2969.
(29) Blankschtein, D.; Thurston, G. M.; Benedek, G. B. Phenomenological theory of equilibrium thermodynamic properties and phase separation of micellar solutions. *J. Chem. Phys.* **1986**, *85*, 7268−7288.




https://doi.org/10.1021/acs.chemmater.6c00541
*Chem. Mater.* XXXX, XXX, XXX−XXX